Whole-Body Contact Sensing via Distributed Low-Cost Joint Torque Sensors for Legged Robots

Jared Grinberg[1] and Yanran Ding[1]

***Abstract*— We present a method for detecting and localizing contact on legged robots using distributed low-cost strain-gauge joint torque sensors and a single hip-mounted force-torque (FT) sensor within a momentum-based observer framework. Our custom designed low-cost strain-gauge-based joint torque sensors provide direct measurements at the motor output shaft, bypassing drivetrain friction and eliminating the need for friction models and motor current estimation. Simulation and hardware experiments on a 2-DOF planar test leg demonstrate sub-centimeter contact localization accuracy and force errors below 0.2 N. Torque estimates from our sensors achieved an average 96.4% fidelity to ground truth measurements.**

I. Introduction

Safe and reliable operation of legged robots in complex environments requires comprehensive contact awareness and accurate sensing of environmental interactions [1], [2]. Contact force sensing at the foot has enabled quadruped robots such as ANYmal [3] and the MIT Cheetah series [4] to achieve impressive mobility on challenging terrain by adapting gait timing and force control to measured ground reaction forces. However, end-effector-only sensing cannot detect off-foot collisions on the thigh or shank, potentially leading to undetected impacts and compromised stability. Moreover, ground contact during dynamic motion is transient – stance phases often last only 50–200 ms [5] – so any collision detection must run with low latency and high precision within that interval. Existing joint-level contact sensing strategies fall into three primary categories.

First, researchers have employed motor current as a surrogate for joint torque [1], [6], [7]; this is viable on high–gear-ratio QDD motors because current and torque are roughly proportional, but drivetrain friction, gearbox nonlinearities, and calibration drift introduce bias unless detailed per-joint friction models are maintained.

Second, momentum observers [1], [8] and probabilistic approaches [6], [9] create residual signals to detect unexpected external wrenches, yet localizing the contact point along a serial chain requires either accurate friction compensation or computationally intensive estimation schemes.

Third, external sensing modalities such as tactile skins [10], [11], distributed FT-sensor arrays, or vision-based systems [12], [13] can directly measure contact events, but deploying multiple sensors across every link incurs cost wiring complexity, and vulnerability to damage.

In this work, we combine direct joint torque sensors with a single hip-mounted FT sensor to enable whole-body contact detection. Our strain-gauge-based sensors measure torque directly at the actuator output shafts, bypassing drivetrain friction entirely. This configuration, integrated with a momentum observer, allows to detect and locate impacts on any leg segment without requiring friction modeling or relying on motor-current-estimated torque.

[1]Jared Grinberg and Yanran Ding are with the Department of Robotics, University of Michigan, Ann Arbor, MI - 48109, USA. {grinberg, yanrand}@umich.edu

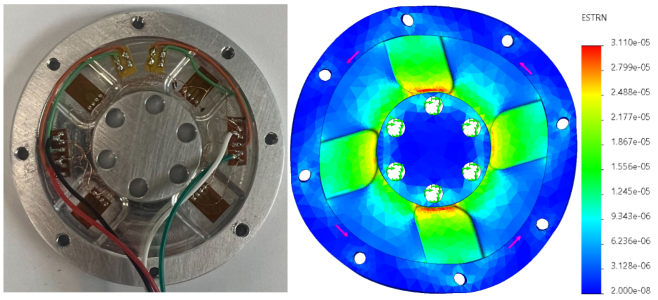

Fig. 1: (Left) Fabricated sensor with strain gauges. (Right) Finite-Element Analysis (FEA) of the custom joint torque sensor under 0.4 Nm load.

II. Background: Momentum-Based Observer

A. Robot Dynamics Formulation

For legged robotic systems, which are underactuated systems unlike fully-actuated manipulators, the dynamics can be described by the equation of motion:

$$\mathbf{M}(\mathbf{q})\,\ddot{\mathbf{q}} + \mathbf{C}(\mathbf{q},\dot{\mathbf{q}})\,\dot{\mathbf{q}} + \mathbf{G}(\mathbf{q}) + \boldsymbol{\tau}_{\text{external}} = \boldsymbol{\tau}_{\text{sensor}}, \quad (1)$$

where $\mathbf{q} \in \mathbb{R}^{N_{\text{total}}}$ collects the generalized coordinates (floating-base $\{x, z\}$ plus N actuated joints), $\dot{\mathbf{q}}, \ddot{\mathbf{q}}$ are velocity and acceleration, $\mathbf{M}$ the inertia matrix, $\mathbf{C}\dot{\mathbf{q}}$ the Coriolis/centrifugal term, $\mathbf{G}$ the gravity vector, and $\boldsymbol{\tau}_{\text{external}}$ any external torque/force mapped into joint space. On the right-hand side, $\boldsymbol{\tau}_{\text{sensor}}$ is our *directly measured* joint torque (post-gearbox), thereby excluding friction effects in the dynamics.

B. Generalized Momentum

Instead of explicitly solving for $\ddot{\mathbf{q}}$, we adopt the momentum-based observer framework from [1], [8]. Define the generalized momentum

$$\mathbf{P} = \mathbf{M}(\mathbf{q})\,\dot{\mathbf{q}}. \quad (2)$$

Taking the time derivative and rearranging [1], [8] yields a *residual*:

$$\mathbf{r}(t) = K\Big[\mathbf{P}(t) - \mathbf{p}_{\text{int}}(t) - \mathbf{P}_0\Big], \quad (3)$$

where K is a gain matrix, $\mathbf{p}_{\text{int}}$ is an integrator state, and $\mathbf{P}_0$ the initial momentum. Discretizing in time yields

$$\mathbf{p}_{\text{int}}(t+\Delta t) = \mathbf{p}_{\text{int}}(t) + \Big[\mathbf{u} + \mathbf{r}(t)\Big]\Delta t. \quad (4)$$

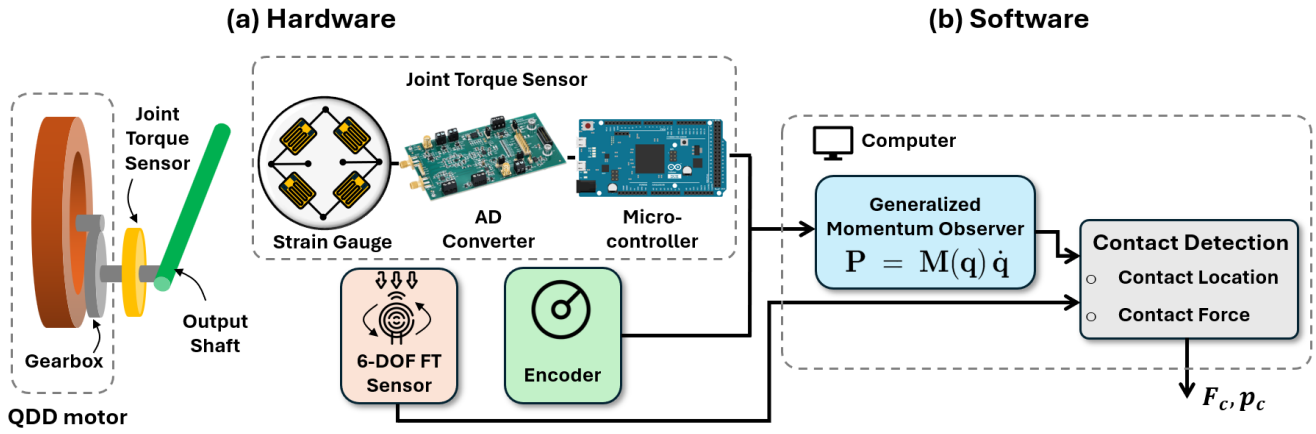

Fig. 2: System schematic depicting data flow for contact detection: (a) motor hardware with joint torque sensors, data acquisition system, and encoders, which feed into (b) a generalized momentum observer sensing algorithm, subsequently input with a 6-DOF force-torque (FT) sensor data for contact detection that outputs estimated contact force and location.

with $\mathbf{u}(t)$ accounting for $\mathbf{C}\dot{\mathbf{q}}$, $\mathbf{G}$, and the measured $\boldsymbol{\tau}_{\text{sensor}}$. When no external torque is present, $\mathbf{r}(t) \approx 0$. A sufficiently large $\|\mathbf{r}(t)\|$ indicates the presence of unexpected external forces.

C. Collision Link Identification

In a serial chain of n links, only the first c joints carry the external force if the collision occurs on link c. Thus, the corresponding observer residual components $r_1, \ldots, r_c$ become nonzero [1], [8]. Formally,

$$r_i(t) \neq 0 \;\text{ for } i = 1, \ldots, c; \; r_j(t) = 0 \;\text{ for } j = c{+}1, \ldots, n. \tag{5}$$

Hence, we identify c by checking which set of consecutive residuals is nonzero.

III. Contact Detection Using Base Wrench and Joint Torque Sensing

Building on the momentum observer described above, we now present our approach to whole-body contact sensing that combines direct joint torque measurements with a hip-mounted FT sensor. This section details the sensing algorithm for contact localization and force estimation and hardware components.

A. Base Wrench Sensing

To localize a collision along the contact link, we leverage a hip-mounted force-torque (FT) sensor that measures the net base wrench $\mathbf{F}_{\text{base}} = \left[F_x^{\text{base}}, F_z^{\text{base}}, M_y^{\text{base}}\right]^\top$. We first compute the residual dynamics term

$$\mathbf{R} = \mathbf{C}(\mathbf{q}, \dot{\mathbf{q}})\,\dot{\mathbf{q}} + \mathbf{G}(\mathbf{q}) - \mathbf{B}\,\boldsymbol{\tau}_{\text{sensor}}, \tag{6}$$

where $\mathbf{B}$ maps the 2D actuated joints into the full coordinate space $\mathbb{R}^{N_{\text{total}}}$. Subtracting the measured base wrench from the portion of $\mathbf{R}$ associated with the base DOFs, we obtain the net *unexpected* wrench:

$$F_i^{\text{unexp}} = R(i) - F_i^{\text{base}}, \quad i \in \{x, z, y\} \tag{7}$$

The planar contact force is

$$\mathbf{F}_c = -\left[F_x^{\text{unexp}},\, F_z^{\text{unexp}}\right]^\top, \tag{8}$$

and imposing zero net moment about the base DOFs gives an algebraic solution for the collision location $\alpha \in [0, 1]$:

$$\alpha = \frac{-M_y^{\text{unexp}} - \left[p_1(1)\,F_z^{\text{unexp}} - p_1(2)\,F_x^{\text{unexp}}\right]}{\left[\Delta x\,F_z^{\text{unexp}} - \Delta z\,F_x^{\text{unexp}}\right]}, \tag{9}$$

where $\Delta x = p_2(1) - p_1(1)$ and $\Delta z = p_2(2) - p_1(2)$ are for the link endpoints $\mathbf{p}_1, \mathbf{p}_2$. If $0 \leq \alpha \leq 1$, the contact is on the link; otherwise, we conclude the force lies out-of-bounds.

B. Joint Torque Sensing

Each joint output shaft is equipped with a strain-gauge-based torque sensor, using a full Wheatstone bridge (1 kΩ gauges at 5 V excitation) on a 6061 aluminum flexure. We model the strain-gauge sensitivity based on:

$$\frac{\Delta R}{R} = \text{GF}\,\epsilon, \quad V_o = V_{\text{ex}} \times \frac{\Delta R/R}{4} \quad \text{(quarter-bridge)}, \tag{10}$$

where $\text{GF} = 2$ is the gauge factor, ϵ is the strain, and $V_{\text{ex}} = 5\,\text{V}$ is the excitation. The sensor's *bridge sensitivity* is $S = V_o/\epsilon$. We employ a 24-bit ADC with a reference voltage of $V_{\text{ref}} = 2.5\,\text{V}$. Although it has a nominal resolution of LSB $= V_{\text{ref}}/2^{24}$, practical noise considerations yield an effective number of bits (ENOB) around 16. Consequently, the theoretical minimal detectable strain becomes

$$\epsilon_{\min} = \frac{4\,V_{\text{ref}}}{\text{GF}\,V_{\text{ex}}\,2^N} \approx 5.96 \times 10^{-8} \quad \text{(ideal)}, \tag{11}$$

but rises to $\sim 1.53 \times 10^{-5}$ when accounting for ENOB. Finite-Element Analysis (FEA) of the aluminum disc shows that expected strains under typical torques of (ideal = 0.001; ENOB = 0.4 Nm) comfortably fall within this detectable range.

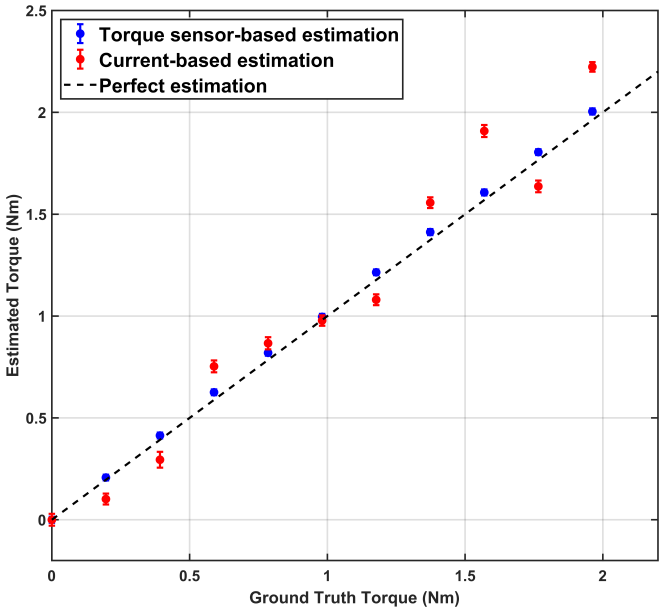

Fig. 3: Comparison of joint torque sensor (blue) versus motor current estimation (red) against ground truth torque. The joint torque sensor provides higher accuracy (R^2 = 0.9998, MAE = 0.0286 Nm) compared to motor current estimates (R^2 = 0.9609, MAE = 0.1319 Nm).

To validate our sensor design, we performed calibration (10 g to 1000 g load range) and verified linearity of the sensors' responses:

$$y = 0.0115\,x + 5.0069, \qquad \text{with } R^2 = 0.9991, \qquad (12)$$

$$y = -0.0108\,x - 2.3260, \qquad \text{with } R^2 = 0.9999, \qquad (13)$$

confirming minimal hysteresis and good repeatability, and maximum gauge differential amplitude output of ∼10 mV. Figure 1 shows the sensor design and FEA results under 0.4 Nm.

Compared to motor current estimates from a QDD motor, our direct joint torque sensing avoids frictional uncertainties and achieves 96.4% fidelity to ground truth measurements, see Figure 3. While both approaches work for moderate loads (0–2 Nm), direct torque sensing yields both lower average errors and smaller variance.

Base Force-Torque Sensor: A six-axis PixONE FT sensor (Bota Systems) is mounted at the hip, using only its planar components (F_x, F_z, M_y) to measure the net external wrench on the 2-DOF limb.

C. Summary of Estimation Procedure

In real-time operation, we compute the momentum-based residual $\mathbf{r}$ (3) and detect a collision once $\|\mathbf{r}(t)\|$ crosses a threshold. We then identify the impacted link by checking which residual components are nonzero (5). Next, we form the "unexpected" wrench from (7) and solve (9) to find the contact location α along that link. This yields both the contact force $\mathbf{F}_c$ and the point p_c. In our 2-link setup, if $|r_2(t)|$ is small while $|r_1(t)|$ is large, the collision is on link 1; otherwise, if both are large, it is on link 2.

IV. Simulation Study

We tested our multi-link contact detection framework in a planar simulation to quantify force and location estimation errors under controlled conditions before proceeding to hardware validation.

1) Performance Metrics: We compare the *true* contact force/location $(\mathbf{F}_{\text{true}}, \alpha_{\text{true}})$ to the *estimated* $(\mathbf{F}_{\text{est}}, \alpha_{\text{est}})$. We report force error $\|\mathbf{F}_{\text{est}} - \mathbf{F}_{\text{true}}\|$ and location error $|\alpha_{\text{est}} - \alpha_{\text{true}}|$.

2) Representative Results: We tested two collision scenarios:

- a 5 N force on link 1 at $\alpha = 0.5$, oriented at $-\pi/3$;
- a 7 N force on link 2 at $\alpha = 0.8$, also at $-\pi/3$;

Tables I and II summarize the robot's physical constants (e.g., link lengths/masses) and simulation parameters (e.g., spring-damper gains, PD gains, sensor noise, and momentum threshold). The threshold $\epsilon_{res} = 0.06$ was chosen empirically from no-contact data in hardware tests.

TABLE I: Physical constants of the robot

Constant	Value	Unit
l	[0.205, 0.215]	m
r	[0.171, 0.031]	m
m	[0.351, 0.080]	kg
I	[0.00207, 0.00030]	kg·m^2
m_{base}	0.738	kg
μ	0.3	\

TABLE II: Simulation and control parameters

Parameter	Value	Unit
K_b	[5000, 5000, 500]	N/m
D_b	[50, 50, 20]	Ns/m
K_P	500	\
K_D	10	\
σ_{FT}	[0.1, 0.1, 0.01]	[N, N, Nm]
ϵ_{res}	0.06	\

A. Floating-Base Simulation

We validate our collision detection algorithm in a floating-base 2-DOF simulation (Fig. 4c) using `ode45` with a 1 kHz PD controller. Collisions of 5–7 N are introduced at various link locations and times, as shown in Figures 4a, 4b. The method achieves 2–5 mm localization error and 0.121–0.162 N force error, see Table III.

TABLE III: Error Metrics During Collision Phase in Floating-Base Simulation

Scenario	Force Errors (N)			Position Errors (m)		
	Fx	Fz	$\|\mathbf{F}\|$	p_x	p_z	$\|\mathbf{p}\|$
Test 1 Mean	-0.033	0.051	0.162	-0.001	0.000	0.005
STD	0.340	0.379	0.486	0.008	0.002	0.007
Test 2 Mean	-0.036	0.050	0.121	-0.001	0.000	0.002
STD	0.313	0.236	0.378	0.004	0.001	0.003

V. Hardware Experiments

Expanding on our simulation results under real-world conditions, we implemented our contact detection approach on physical hardware. This section describes the experimental setup and presents results comparing estimated versus ground-truth contact forces and locations.

A. Fixed-Base Experiment

To verify the system's collision-estimation accuracy under real-world conditions, we implement our approach on a physical *fixed-base* 2-DOF planar linkage equipped with joint torque sensors and a hip-mounted FT sensor, as shown in Figure 5.

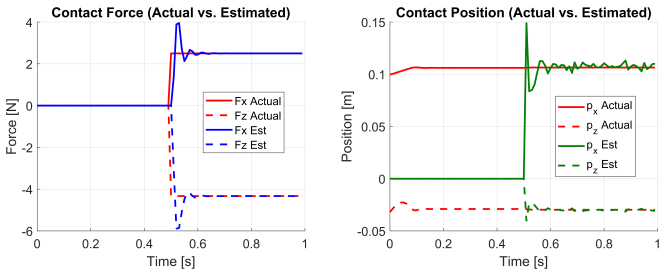

(a) Floating Base, Scenario 1: Collision on Link 1 (5 N, $\alpha = 0.5$)

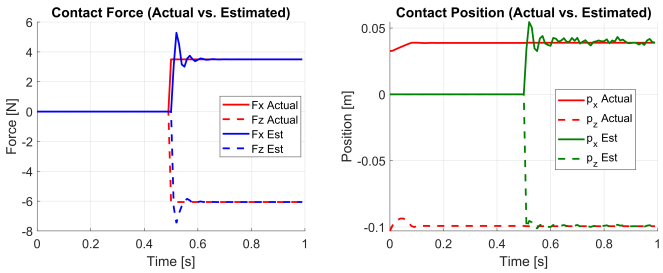

(b) Floating Base, Scenario 2: Collision on Link 2 (7 N, $\alpha = 0.8$)

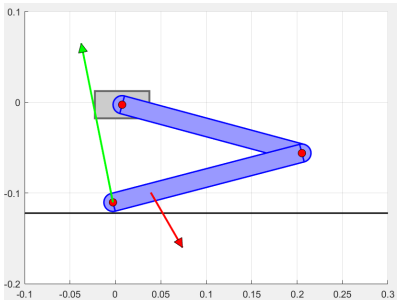

(c) Simulation setup for the floating-base 2-DOF leg. Red arrow: external poking force applied to the link; green arrow: ground-contact reaction force at the foot. Both arrows are uniformly scaled (0.01x) for visualization.

Fig. 4: Floating-base collision detection: (a,b) actual vs. estimated contact force magnitude and location; (c) setup showing external (red) and ground-contact (green) forces.

1) Data-Acquisition Pipeline: All torque sensors feed into a dedicated 24-bit ADC module (ADS127L21EVM-PDK) via an Arduino Due communicating over SPI. The ADC transmits the readings at 2 MHz baud rate, yielding a sampling rate of 3–4 kSps. Meanwhile, mjbots controllers supply encoder data, and a Bota Systems PixONE FT sensor sends base wrench measurements. All streams are synchronized in MATLAB for real-time observer computations, with an mjbots qdd100 (6:1) and mj5208 direct drive for actuation.

2) Static Loading Tests and Accuracy Evaluation: To quantify force and location estimation, we perform static loading by placing known masses at specific positions along each link. Specifically, we tested Link 1 (thigh) with 100 g and 500 g loads and Link 2 (shank) with 50 g and 100 g loads, each at 25%, 50%, 75%, and 100% of link length. Link 1 errors ranged from 7–9 mm, while Link 2 errors stayed around 4–5 mm. Force errors remained below 0.2 N, shown in Table IV.

For comparison, we also test the fixed base system in simulation, where we emulate a FT sensor by modeling the planar robot's floating base with virtual spring-damper

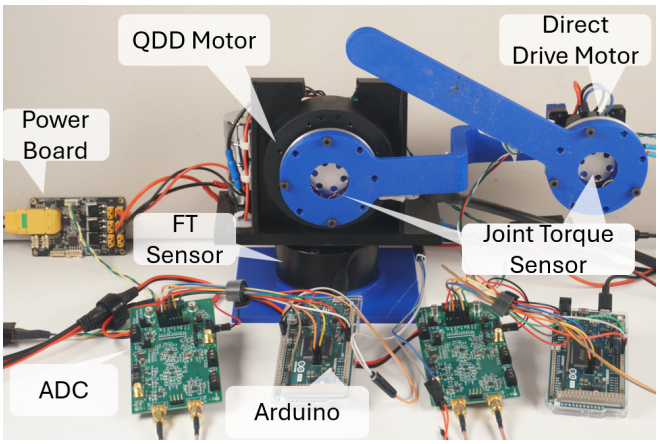

Fig. 5: Experimental 2-DOF planar leg testbed with integrated joint torque sensors, data acquisition boards, a hip-mounted Bota Systems PixONE FT sensor, and power distribution board.

TABLE IV: Error Metrics in Hardware Experiments

Configuration	Load (g)	Location Error RMS (mm)	Force Error RMS (N)
Link 1	100	8.89	0.129
	500	7.91	0.174
Link 2	50	4.09	0.045
	100	4.87	0.106

elements in (x, z, θ). This test yield similarly low errors (Table V), confirming the observer's consistency. The floating-base simulation in Section IV appears to result in higher variance measurements, which could be caused by the system stabilizing after the contact occurred.

TABLE V: Error Metrics During Collision Phase in Fixed-Base Simulation

Scenario	Force Errors (N)			Position Errors (m)		
	Fx	Fz	$\lvert\mathbf{F}\rvert$	p_x	p_z	$\lvert\mathbf{p}\rvert$
Test 1 Mean	-0.008	-0.008	0.112	0.001	0.000	0.003
STD	0.089	0.090	0.058	0.004	0.001	0.002
Test 2 Mean	0.002	-0.006	0.142	0.000	0.002	0.002
STD	0.108	0.111	0.059	0.002	0.001	0.001

To evaluate robustness across different leg configurations, we swept joint angles (q_1, q_2) over a 10×10 grid in $[0, \pi] \times [0, \pi]$, placing contacts at four points along each link. Across all configurations, the collision location error stayed below 13.5 mm (about 7% of the link length) and force error under 0.15 N ($\sim$ 2%). Thus, our observer consistently maintains sub-centimeter precision regardless of leg posture.

VI. Discussion and Conclusion

Our simulation and 2-DOF hardware tests confirm combining direct joint torque sensing with a single hip-mounted FT sensor enables multi-link collision detection and localization, even under friction and gearbox uncertainties. Key findings include: Torque estimates achieving 96.4% fidelity to ground truth compared to motor-current methods, sub-centimeter contact localization precision in fixed-base and floating-base scenarios, and force measurement errors below 0.2 N across varied scenarios.

Future work will embed this sensing architecture into 3D, higher-DOF legged robots and dynamics gaits, paving the way for low-latency, whole-body collision awareness on fast, agile platforms.

REFERENCES

[1] S. Haddadin, A. De Luca, and A. Albu-Schäffer, "Robot collisions: A survey on detection, isolation, and identification," *IEEE Trans. Robotics*, vol. 33, no. 6, pp. 1292–1312, 2017.

[2] M. Iskandar, A. Albu-Schäffer, and A. Dietrich, "Intrinsic sense of touch for intuitive physical human-robot interaction," *Science Robotics*, 2024.

[3] M. Hutter, C. Gehring, A. Lauber, F. Gunther, D. C. Bellicoso, V. Tsounis, J. Hwangbo, and R. Siegwart, "Anymal – toward legged robotics for harsh environments," *Advanced Robotics*, vol. 31, no. 17, pp. 918—931, 2017.

[4] J. Di Carlo, P. M. Wensing, B. Katz, G. Bledt, and S. Kim, "Dynamic locomotion in the MIT cheetah 3 through convex model-predictive control," in *Proc. IEEE/RSJ Int. Conf. on Intelligent Robots and Systems (IROS)*, 2018, pp. 7440–7447.

[5] M. A. Daley and A. A. Biewener, "Running over rough terrain reveals limb control for intrinsic stability," *Proc. National Academy of Sciences (PNAS)*, vol. 103, no. 42, pp. 15 681–15 686, 2006.

[6] D. Zurlo, A. De Luca, T. Heitmann, and M. Morlock, "Collision detection and contact point estimation using combined energy and momentum methods," in *Proc. IEEE Int. Conf. on Robotics and Automation (ICRA)*, 2023, pp. 7533–7539.

[7] D. P. Le, J. Choi, and S. Kang, "External force estimation using joint torque sensors and its application to impedance control of a robot manipulator," in *Proc. 13th Int. Conf. on Control, Automation and Systems (ICCAS)*, 2013, pp. 1794–1798.

[8] A. De Luca and R. Mattone, "Sensorless collision detection and reaction for robot manipulators," in *Proc. IEEE Int. Conf. on Robotics and Automation (ICRA)*, 2005, pp. 999–1004.

[9] L. Manuelli and R. Tedrake, "Localizing external contact using proprioceptive sensors: The contact particle filter," in *Proc. IEEE/RSJ Int. Conf. on Intelligent Robots and Systems (IROS)*, 2016, pp. 5062–5069.

[10] G. Cheng, E. Dean-Leon, F. Bergner, J. R. G. Olvera, Q. Leboutet, and P. Mittendorfer, "A comprehensive realization of robot skin: Sensors, sensing, control, and applications," *Proc. IEEE*, vol. 107, no. 10, pp. 2034–2051, 2019.

[11] I. S. Bayer, "Mems-based tactile sensors: Materials, processes and applications in robotics," *Micromachines*, vol. 13, no. 12, p. 2051, 2022.

[12] A. SaLoutos, E. Stanger-Jones, M. Guo, H. Kim, and S. Kim, "Design of a multimodal fingertip sensor for dynamic manipulation," in *Proc. IEEE Int. Conf. on Robotics and Automation (ICRA)*, 2023, pp. 8017–8024.

[13] W. Yuan, S. Dong, and E. H. Adelson, "GelSight: High-resolution robot tactile sensors for estimating geometry and force," *Sensors*, vol. 17, no. 12, p. 2762, 2017.